Breaking Scaling Relationships in CO_2 Reduction on Copper Alloys with Organic Additives

Yungchieh Lai,[#] Nicholas B. Watkins,[#] Alonso Rosas-Hernández, Arnaud Thevenon, Gavin P. Heim, Lan Zhou, Yueshen Wu, Jonas C. Peters,* John M. Gregoire,* Theodor Agapie*
Division of Chemistry and Chemical Engineering, California Institute of Technology, Pasadena, CA, 91125, USA. [#]These authors contributed equally to this work. *e-mail: jpeters@caltech.edu; gregoire@caltech.edu; agapie@caltech.edu

Supporting Information

Table of Contents

Material Synthesis

Cu thin film electrocatalysts were fabricated using DC magnetron sputtering of a 2" Cu metal target at 50 W in 6 mTorr Ar onto a 100 mm-diameter Si wafer with an approximately 170 nm SiO_2 diffusion barrier and 10 nm Ti adhesion layer, using a previously described sputter system with 10-5 Pa base pressure.[1] After deposition, the films were stored in a nitrogen purge box until the day of electrochemical testing, although no other catalyst treatment was performed prior to electrocatalyst screening. The Cu-X (X: Co, Zn, Mn, In) thin film electrodes were deposited under similar conditions from elemental metal targets with DC power adjusted to obtain designed composition in the wafer center. All the metal targets were pre-cleaned in the presence of 6 mTorr Ar for 10 min to remove any contaminants from the target surface. The non-confocal sputtering geometry provided a continuous composition gradient across the Si wafer with the composition variation within each 5 mm diameter electrode being less than 1% for the most Cu-rich catalysts and about 2% for the most Cu-poor catalysts.

Electrochemistry

ANEC Analytical and Electro-chemistry (ANEC) is an analytical electrochemistry system previously published by our group that can efficiently detects a wide range of CO_2R product.[2] This system is applied in this study to further explore those Cu-X catalysts that are representative of the primary conclusions. Prior to the electrolysis, the electrolyte 0.1 or 0.25 M Potassium bicarbonate (>= 99.95% trace metals basis) with or without 0.1 mM **1-Br_2** was purged with CO_2 (99.999%, Airgas) for at least 30 min. A bipolar membrane (Fumasep® FBM single film, Fumatech) was used to separate the working and counter electrodes. Platinum wire (99.9%, Sigma Aldrich) was used as the counter electrode. The surface area of the counter electrode was about 0.25 cm^2, while the working electrode surface area was 0.32 cm^2. The working electrode chamber has headspace volume ~3.3 ml and electrolyte volume ~1.1 ml which is the optimized ratio to maximize product concentration for detection.[2] Electrolysis was carried out with a Gamry Reference 600™ potentiostat. The uncompensated solution resistance was measured by performing electrochemical impedance spectroscopy (EIS) in the frequency range of 100 Hz to 500 kHz with an amplitude of 10 mV at the open circuit potential of a Pt-Pt Working Electrode-Counter Electrode system. The uncompensated resistance, Ru, was measured by using a Nyquist plot of the EIS spectra and was found to be 70 and 32 Ohms for 0.1 and 0.25 M $KHCO_3$, respectively. All electrochemical data was collected vs. a Ag/AgCl reference electrode (LF2, Innovative Instruments) and converted to a reversible hydrogen electrode (RHE) scale. Prior to electrolysis, a constant potential at -1 V vs RHE (without IR compensation) was conducted as pretreatment for each composition of the library. Since the co-sputtered plate was used as is (unlike Cu foil which would be polished prior to tests), such pre-electrolysis was performed to 1) reduce any impurity oxide on the surface and 2) to pre-deposit additives on the surface. To be consistent, 15 min CA was applied to all libraries tested. Electrolyses were then performed at constant potentials (chronoamperometry) mostly between -0.9 to -1.3 V vs RHE (without IR compensation). While electrolysis, the electrolyte was recirculated to quickly accumulate reaction product for detection at a flow rate ~150 uL/s. This high flow rate, compared to other flow cells reported for CO2R (typically with 1-2 uL/s), creates an environment for less mass transport limitations.[3] It is noted that any electrolysis tests associated with additive electrolytes used is in the presence of 0.1 mM **1-Br_2**. The duration for electrolysis typically ranging from 5 to 15 mins depends on the total current of each test to maximize the concentration of reaction product while maintaining high throughput experimentation and avoiding pH hikes in the case >5% of CO_2 in the headspace is consumed.[2] To assure this varying reaction durations will not change the product ratios, we do multiple tests on one Cu sample with different

CA durations and range it from 3 to 15min. The results show CO2R products grow linearly with time, for example, Figure S11 shows $[CH_4]/[C_{2+}]$ remains constant at this time range. At the end of each electrolysis, gaseous and liquid products were sampled by the robotic sample handling system (RSHS) and analyzed by GC (Thermo Scientific™ TRACE™ 1300) and HPLC (Thermo Scientific UltiMate 3000). Detailed product detection (method) can be found at the previous publication.[2] The cell and all solution handling lines are purged with fresh electrolyte and CO_2 between electrolysis to avoid cross-contamination. The actual (compensated) potential shown in this manuscript was corrected with the uncompensated resistance Ru measured above prior to further data analysis.

Experimental Uncertainty

Variation in the current during an electrolysis experiment leads to a variation in the compensated resistance, and the standard deviation thereof is illustrated as horizontal error bars in Figure 2A. For correlation analysis of partial current densities, since each pair of partial current densities result from the same electrolysis, this variation in potential is negligible under the assumption that it does not span multiple kinetic regimes. The uncertainty in partial current density has one contribution from the aliquot and analytic chemistry processes, which we characterize during chromatography calibration for each product. The uncertainty is well modelled as a relative error in each measured concentration, which corresponds to the same relative error in partial current densities. For example, the relative error in CH4 quantification is 2.7%. The relative error in C_{2+} quantification varies depending on the specific combination of products and is between 2% and 7% for all electrolyses reported herein. For every partial current density data point in Figures 2a, 2b, 2c, and 2f, the corresponding error bars are smaller than the marker size. While this sampling error is negligible, more substantial sources of variability in measured partial current densities may result from the impacts of turbulent flow, bubble occlusion of part of the working electrode, etc., which are unquantified in the present work. Rather than perform many repetitions of a single experiment to quantify this variability, we perform a breadth of experiments to better characterize the universality of the relationships, where a large unquantified uncertainty would obscure the observation of correlations or other relationships; fortunately, this is not the case.

Influence of Local pH

Local pH is important for CO_2R product distribution, however, our current cell is not capable of measuring the pH at the electrode surface. It is particularly difficult to accurately measure the pH of the microenvironment at the catalyst surface and would be a significant challenge to take these measurements. However, given the rapid flow condition, a substantial pH change will be limited to the diffusion layer and will be driven by the total current density. Therefore, an indirect study of any influence of pH shift can be made by evaluating whether the current density is related to the observed product ratio. The Figure S18 shows that the current density is not a primary determinant of the product ratio.

Impact of [CO] on CH_4 and C_{2+} formation

Since *CO is understood to be the precursor for both CH_4 and C_{2+} products, as opposed to formic acid per various mechanisms reported in the literature, we specifically investigate whether there is evidence of molecular CO being a reactant for CH_4 and C_{2+} formation.[4,5] Figure S19 shows the corresponding partial current densities as a function of the [CO], showing no systematic relationship and especially not a strong positive correlation that would result from CO reduction being a significant source of these products. In the presence of the additive, the negative correlation between CO and both CH_4 and C_{2+} shows that the competition for the common *CO intermediate is more prominent than CO reduction. In the time-dependent measurements (Figure S11), the proportionality of both CH_4 and C_{2+} with electrolysis time for Cu further corroborates that CO reduction is insignificant. This finding is also intuitive in the context of the concentration data shown in Figure S19, where a ~2% maximum CO concentration corresponds to a partial pressure of 0.02 atm of CO that equilibrates to 0.02 atm * 9.5E-4 mol/L/atm = 19 μM, more than 1000× less than the concentration of dissolved CO_2 (~32 mM).

With a given population of *CO that may or may not be equilibrated with a local aqueous [CO], Figure 3A illustrates that the reactions pathways fall into 3 important categories labelled by the resulting (measured) products: CO, CH_4 and C_{2+}. For a given catalyst and potential there is some branching ratio for each of these paths. There is limited literature regarding whether the relative free energy barriers for these products could be changed independently. Since CO production can vary drastically without a systematic change in the other two types of products, there is an implication that no free energy scaling relationship exists between CO and either CH_4 or C_{2+} products. Those null results are equally important observations as the scaling relationship that we did identify, although each null result demonstrates that there is not a necessary mechanism to break that (nonexistant) scaling relationships. Hence the focus in this report on the CH_4-C_{2+} relationship and its disruption via addition of 1-Br_2. Although we find no evidence of a CO-CH_4 or CO-C_{2+} power law relationship, these products are linked through their common intermediates, which is most evident in the presence of the additive where a negative correlation coefficient indicates the kinetic competition for the intermediate.

Material Characterization

The bulk compositions of the Cu-X alloys were characterized via x-ray fluorescence (XRF, EDAX Orbis MicroXRF). The composition of all the alloys screened is shown in table S1. Additional XRD characterization shown in Figures S12-16.

Table S1: Alloy compositions tested in ANEC cell for performance in CO_2 reduction.

Cu	CuMn	CuIn	CuZn	CuCo
–	26.5 : 73.5	–	29.5 : 70.5	–
–	48.5 : 51.5	–	48.7 : 51.3	–
–	–	–	79 : 21	–
–	84 : 16	83.5 : 16.5	87 : 13	83.5 : 16.5
–	97 : 3	–	95.8 : 4.2	96.7 : 3.3
–	–	–	97.0 : 3.0	–
100: 0	98 : 2	97.8 : 2.2	97.4 : 2.6	97.8 : 2.2

Synthetic Procedures

Synthesis of N,N'-ethylene-phenanthrolinium dibromide (**1-Br_2**) In a round bottom flask charged with a magnetic stir bar, phenanthroline (500 mg, 2.8 mmol, 1 equiv.) was dissolved in dibromoethane (5 mL, 67.4 mmol, > 24 equiv.) and the final mixture was heated to 110 °C for 18 h. The precipitate formed was collected by filtration and washed with hexane (3 x 10 mL) and acetone (3 x 10 mL) to afford the final product. Yield: 970 mg (94 %, 2.6 mmol). 1H and 13C NMR spectra were in accordance with reported values.[6]

Raw Data

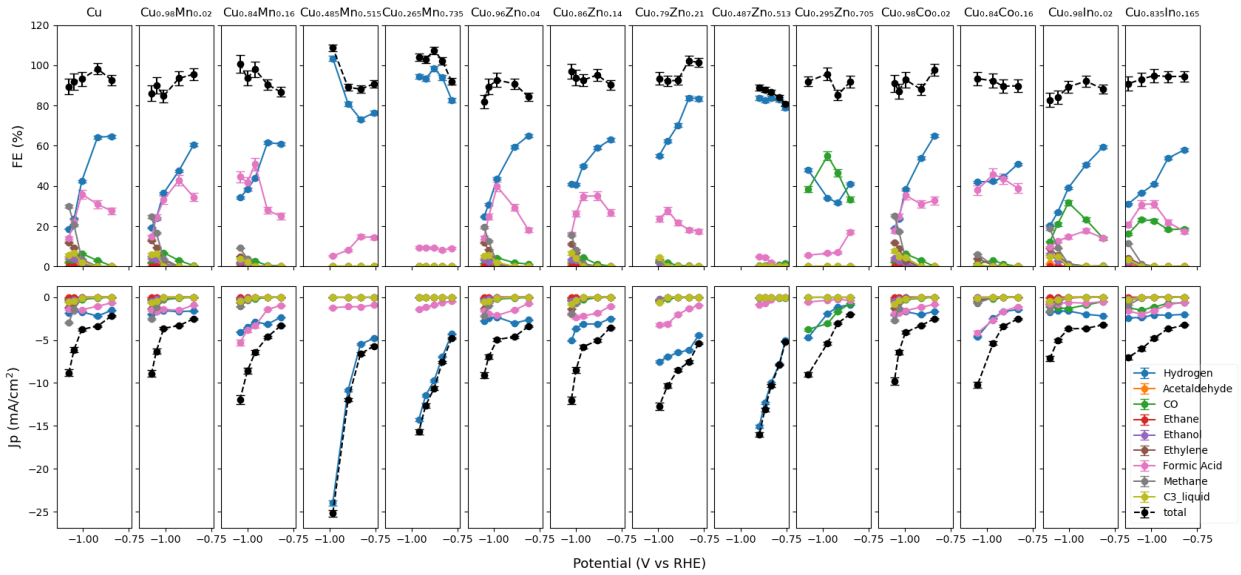

Figure S1: Cu alloy product distribution in the absence of additives in 0.1M $KHCO_3$. The error bars shown in the figure include sampling/leak as well as the analytical instrument calibration errors.

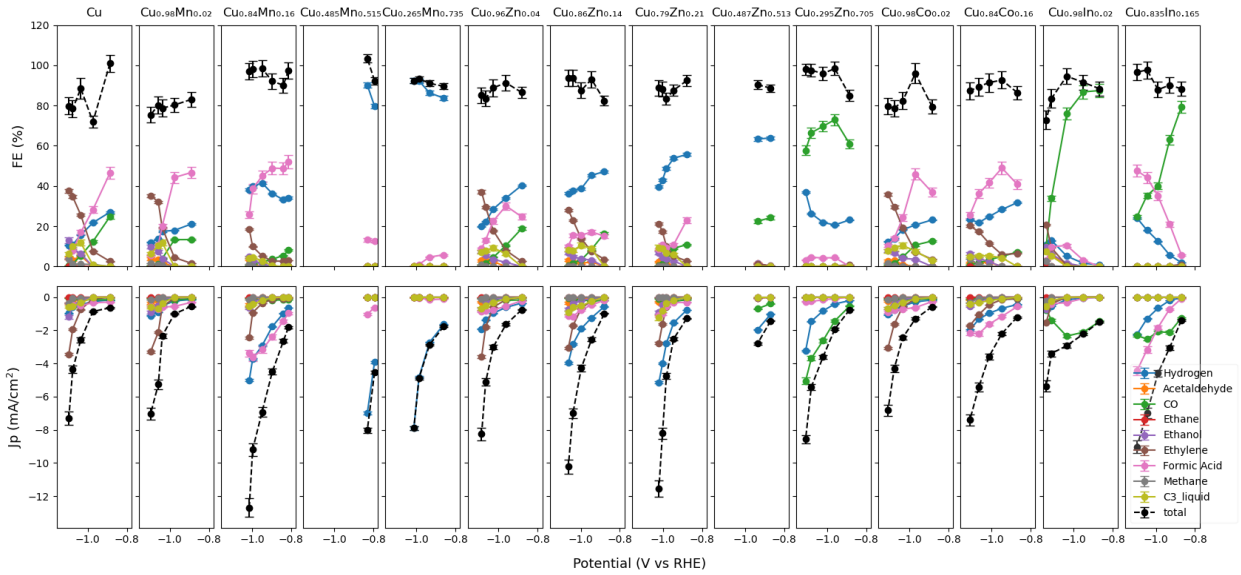

Figure S2: Cu alloy product distribution with 0.1 mM **1-Br$_2$** in 0.1 M $KHCO_3$**.** The error bars shown in the figure include sampling/leak as well as the analytical instrument calibration errors.

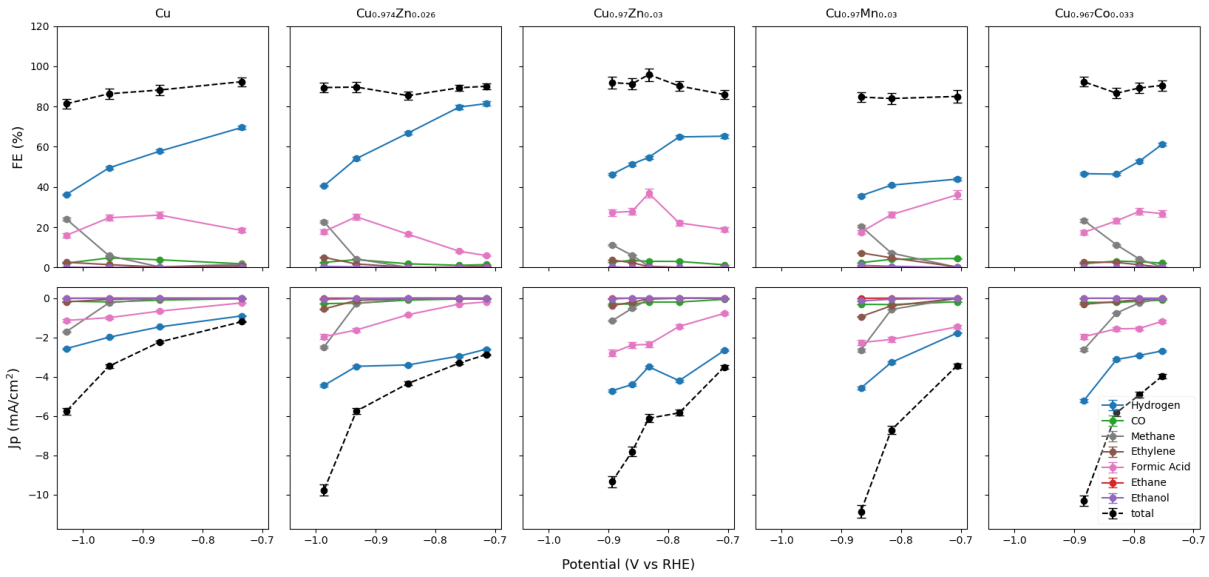

Figure S3: Cu alloy product distribution in the absence of additives in 0.25 M $KHCO_3$ (pH=7.15). The error bars shown in the figure include sampling/leak as well as the analytical instrument calibration errors.

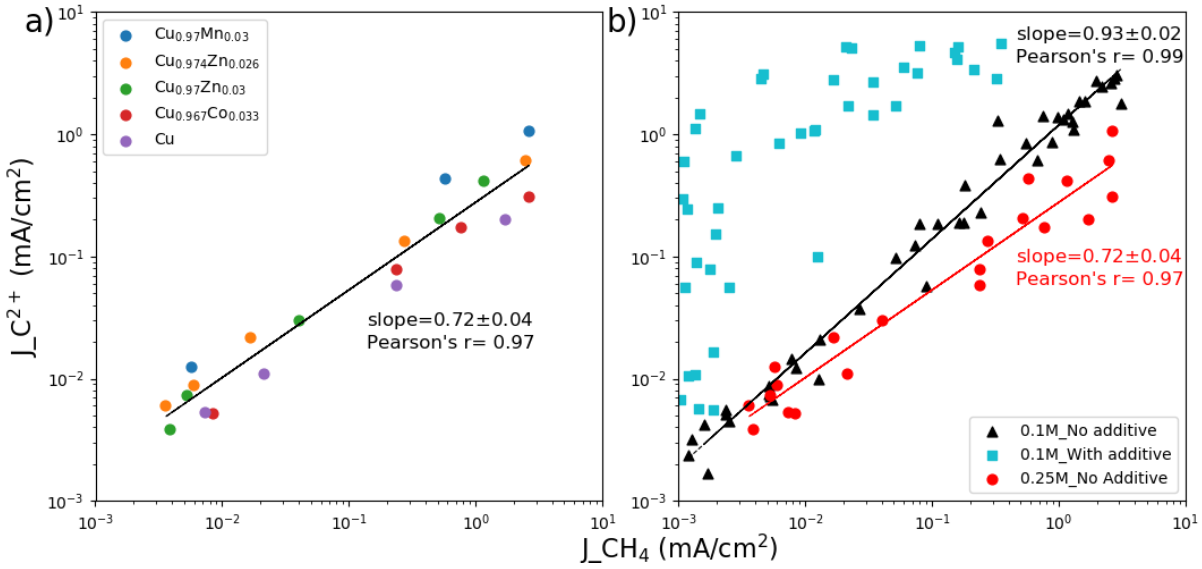

Figure S4: a) The data underlying the correlation analysis from 0.25 M $KHCO_3$. b) Comparison for the trends between 0.1 and 0.25 M $KHCO_3$. The latter shows a relatively gradual slope suggests an increased selectivity toward methane at higher bicarbonate concentrations.

Figure S5: Visualization of the pairwise relationships in the current density (bottom-left) and FE (upper-right). Each data point corresponds to a single catalyst composition and potential. The pairwise relationships are shown for representative reaction products, and in the current density plots the total cathodic current density is also shown.

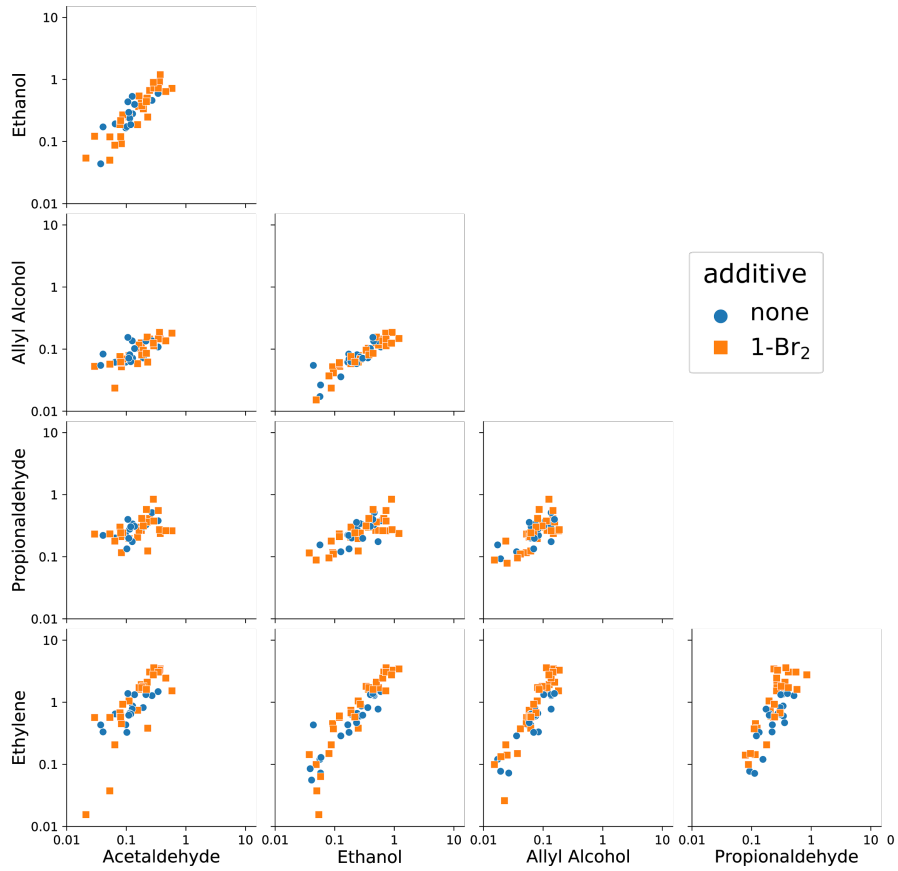

Figure S6: For the 5 prominent C_2 and C_3 products, the 10 pairwise relationships of the partial current densities (mA cm^{-2}) are shown, illustrating a high degree of correlation among these products, both in the presence and absence of the additive, which is expected given common initial pathways for formation of each product.

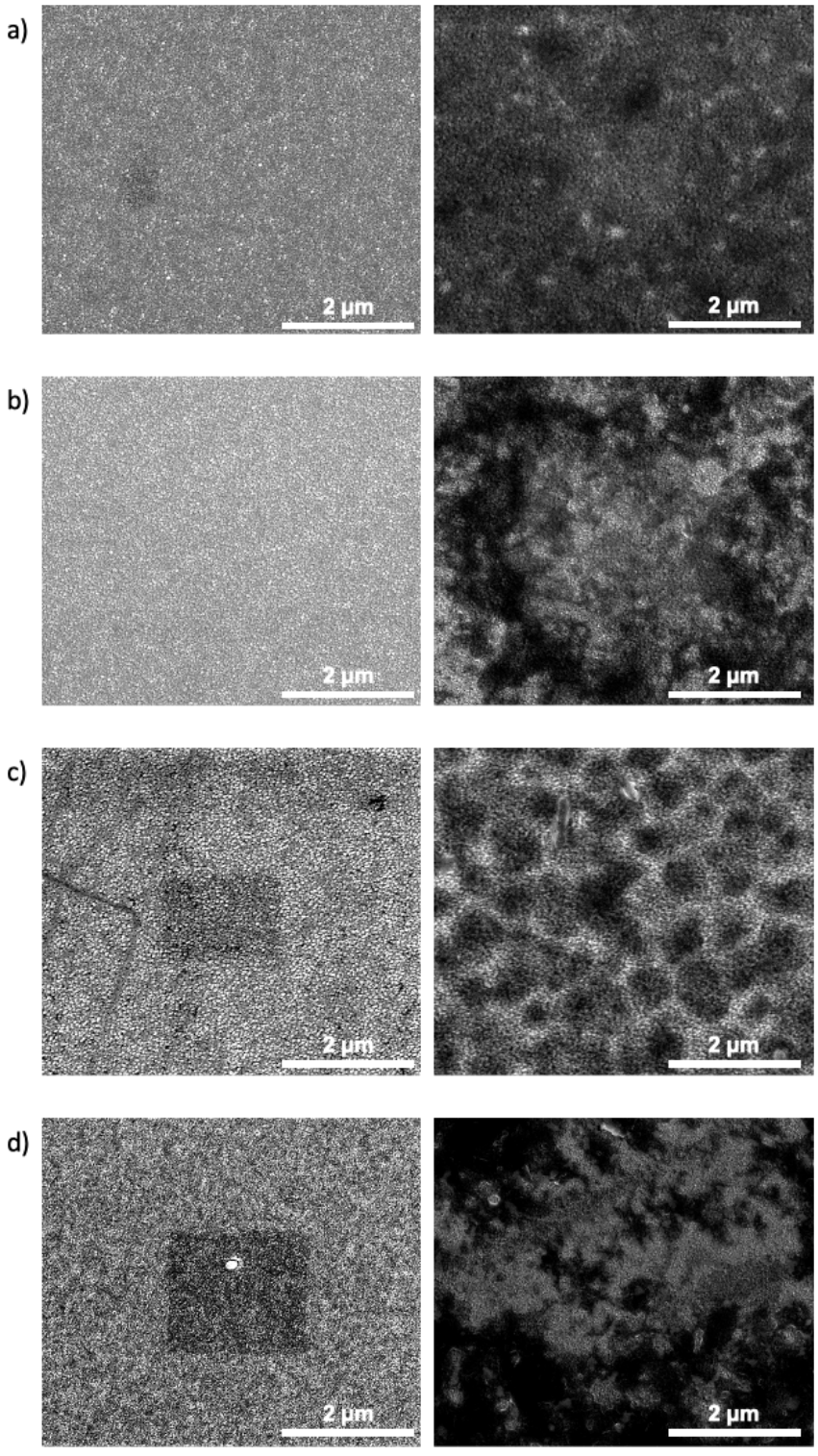

Figure S7: SEM of catalysts before (left column) and after (right column) catalysis with molecular additives. a) CuZn samples b) CuMn samples c) CuIn samples d) CuCo samples. Due to being deposited on SiO_2 disks, charging of the surface with SEM was notable. In the second column with molecular additives, the dark charging regions correspond to additive on the surface. No significant surface restructuring was observed for any catalyst tested. Any texture observed in the right column corresponds to thicker regions of the film on the surface of the catalyst.

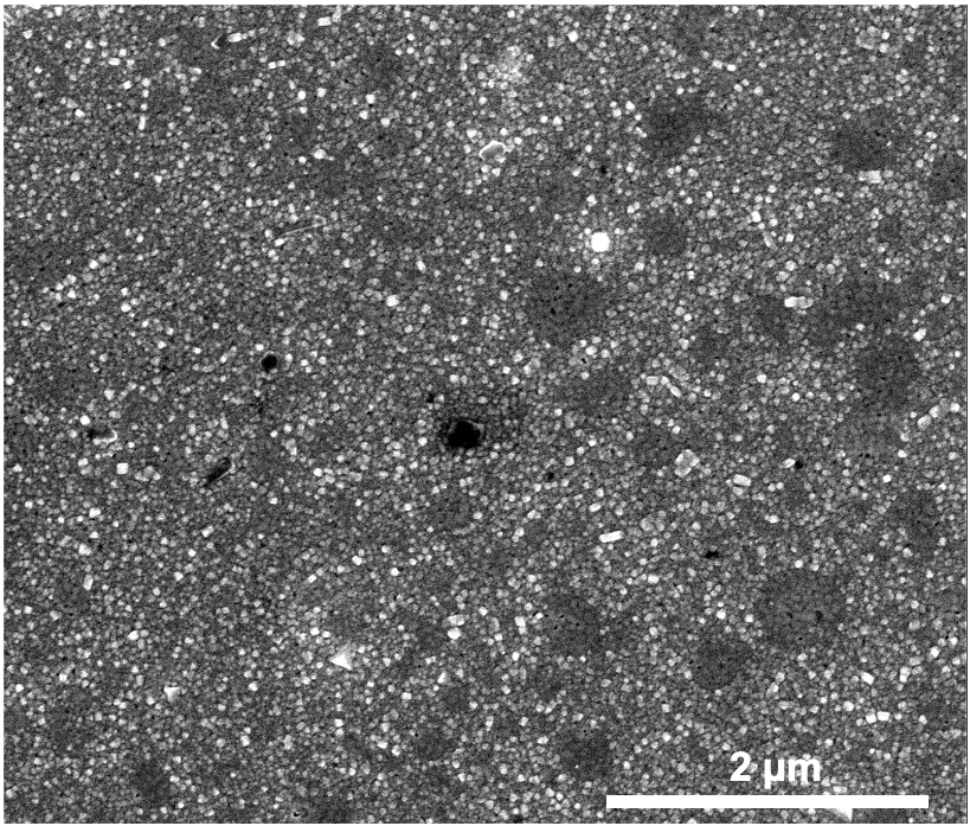

Figure S8: SEM of Cu catalyst after catalysis without molecular additives - no notable nanostructuring is observed.

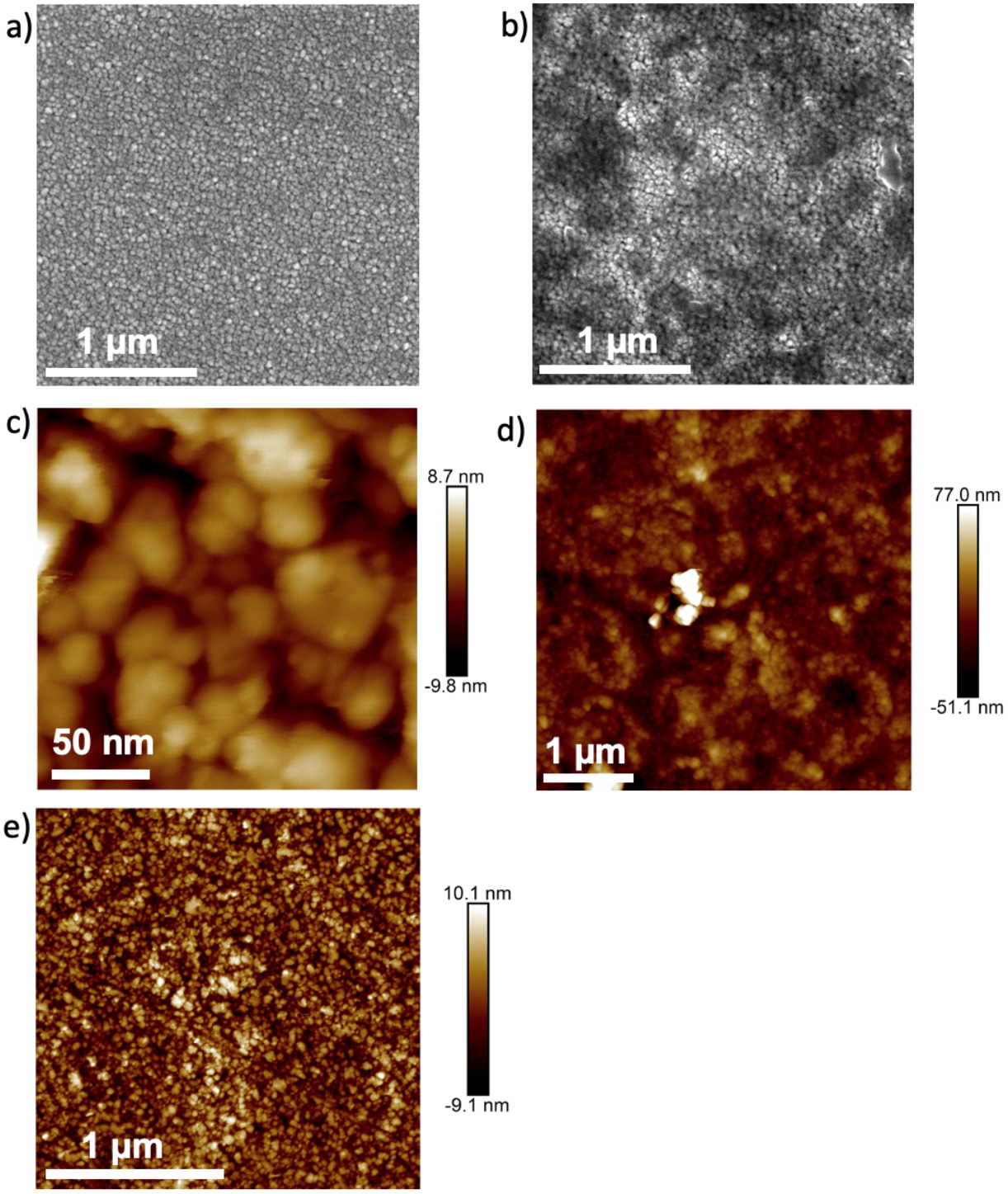

Figure S9: a) Precatalysis SEM of CuMn shows a grain size of 34.2 ± 18.5 nm. b) Zoomed in postcatalysis SEM of CuMn with additive shows there is a film on the surface and the surface structure underneath remains unchanged. c) AFM of precatalysis CuMn with grain size of approximately 40.5 nm. d) Postcatalysis AFM of CuMn with additive shows agglomerated film on surface, as shown by the increase in magnitude of the scale bar. e) AFM of CuMn postcatalysis surface with additive after washing off film shows consistent grain size with the precatalysis surface of approximately 38.7 ± 14.1 nm.

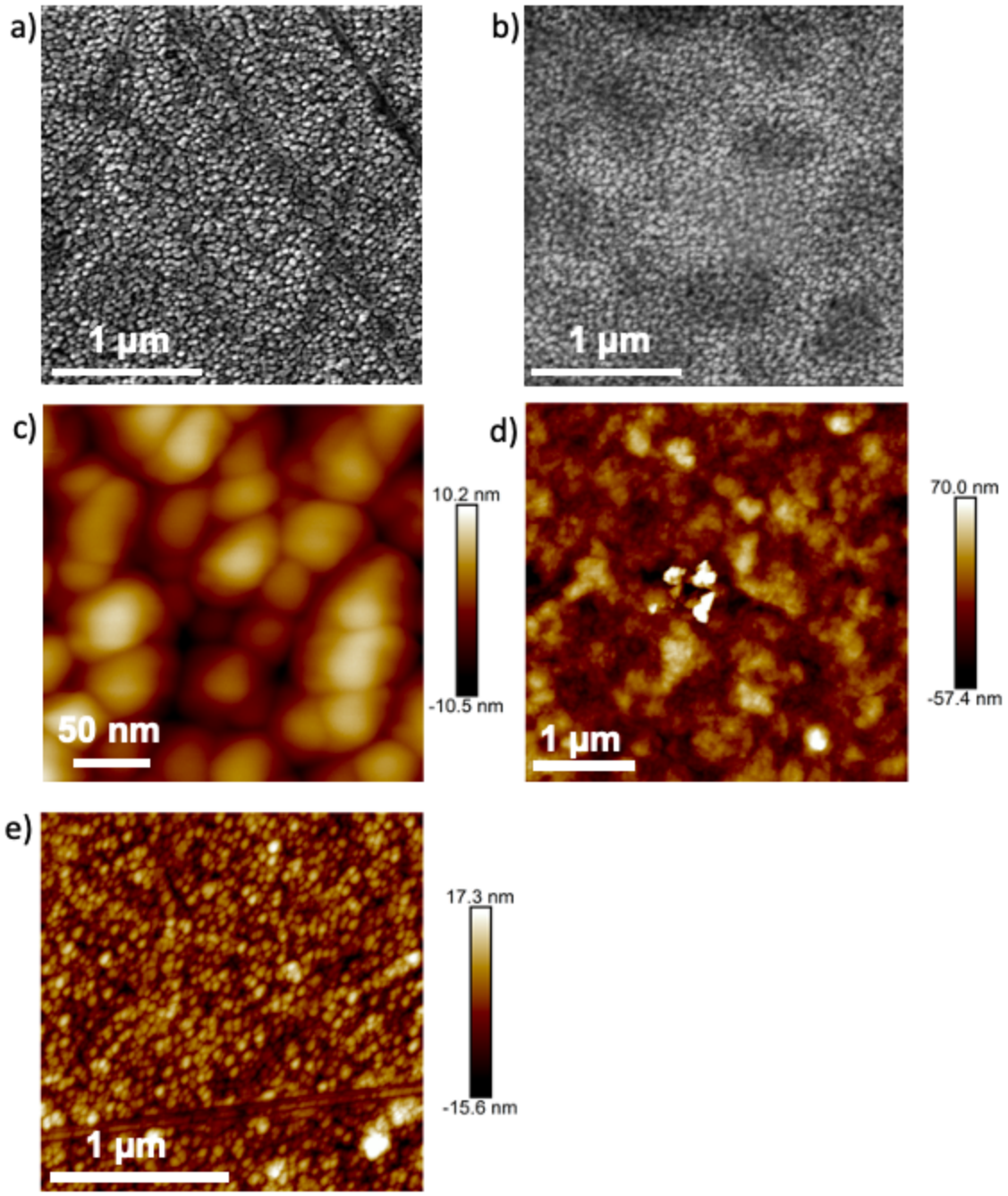

Figure S10: a) Precatalysis SEM of CuIn shows a grain size of 50.2 ± 17.3 nm. b) Zoomed in postcatalysis SEM of CuIn with additive shows there is a film on the surface and the surface structure underneath remains unchanged. c) AFM of precatalysis CuIn has a grain size of approximately 35 nm. d) Postcatalysis AFM of CuIn with additive shows agglomerated film on surface, as shown by the increase in magnitude of the scale bar. e) AFM of CuIn postcatalysis surface with additive after washing off film shows consistent grain size with the precatalysis surface of approximately 37.7 ± 16.0 nm.

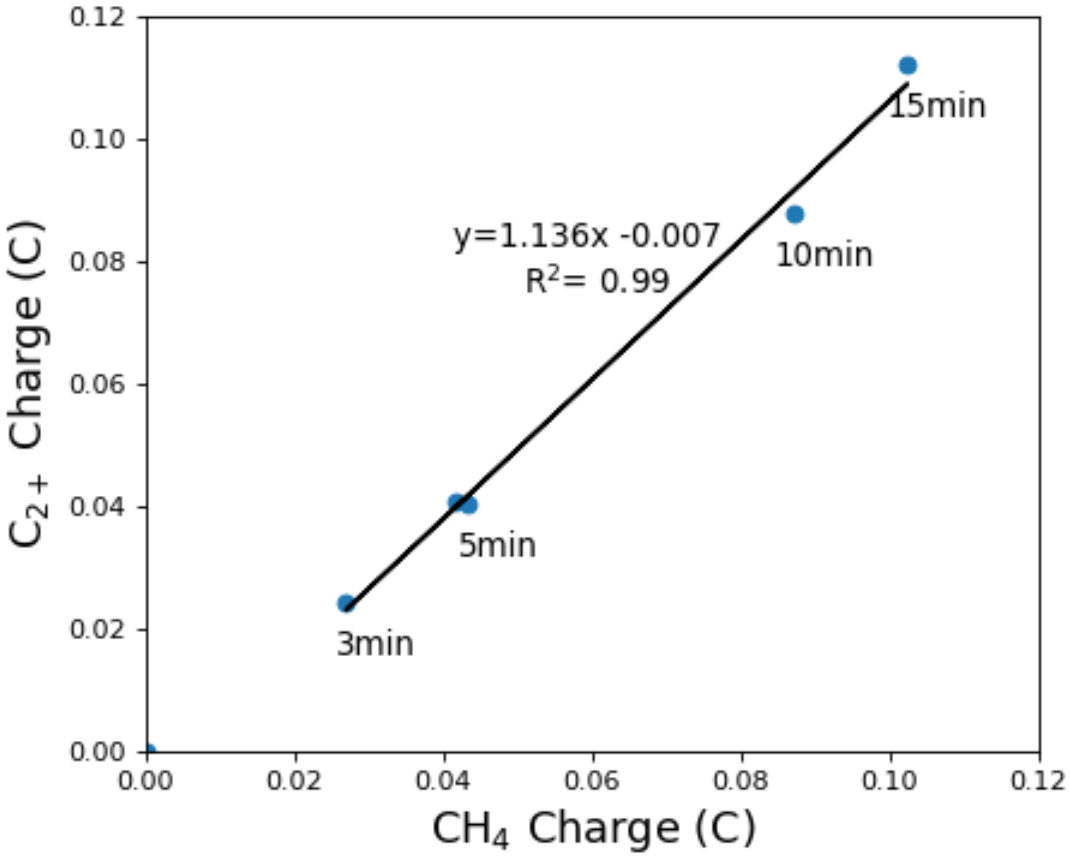

Figure S11: Resulting CH_4 vs C_{2+} from CA at -1.04 V vs RHE with different durations on Cu in 0.1 M $KHCO_3$. The testing sequence was 5, 3, 10, 15, and then 5 mins. The repeated 5 min CA experiment was conducted to check for variation after multiple experimental runs at different duration. The lack of variation at 5 min suggests that the electrode performs consistently and reproducibly over time

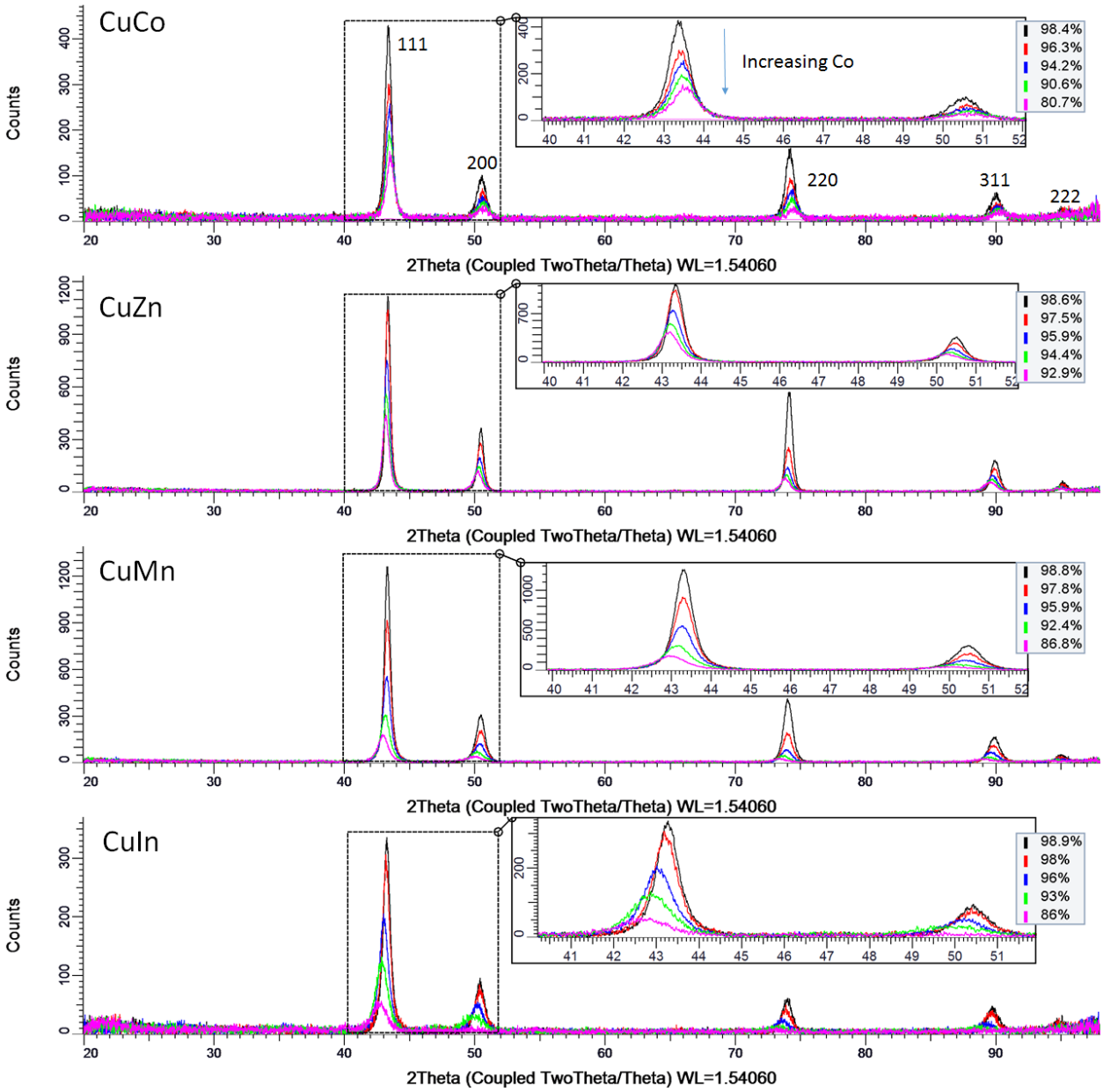

Figure S12: XRD for the as-synthesized alloys investigated. All compositions shown are alloyed cubic Cu structure and are with space group of Fm-3m. For In, Mn, Zn alloys, peaks shift to smaller 2-theta (larger d-spacing) with increasing alloy content. For Co, peaks shift to larger 2-theta (smaller d-spacing) with increasing Co.

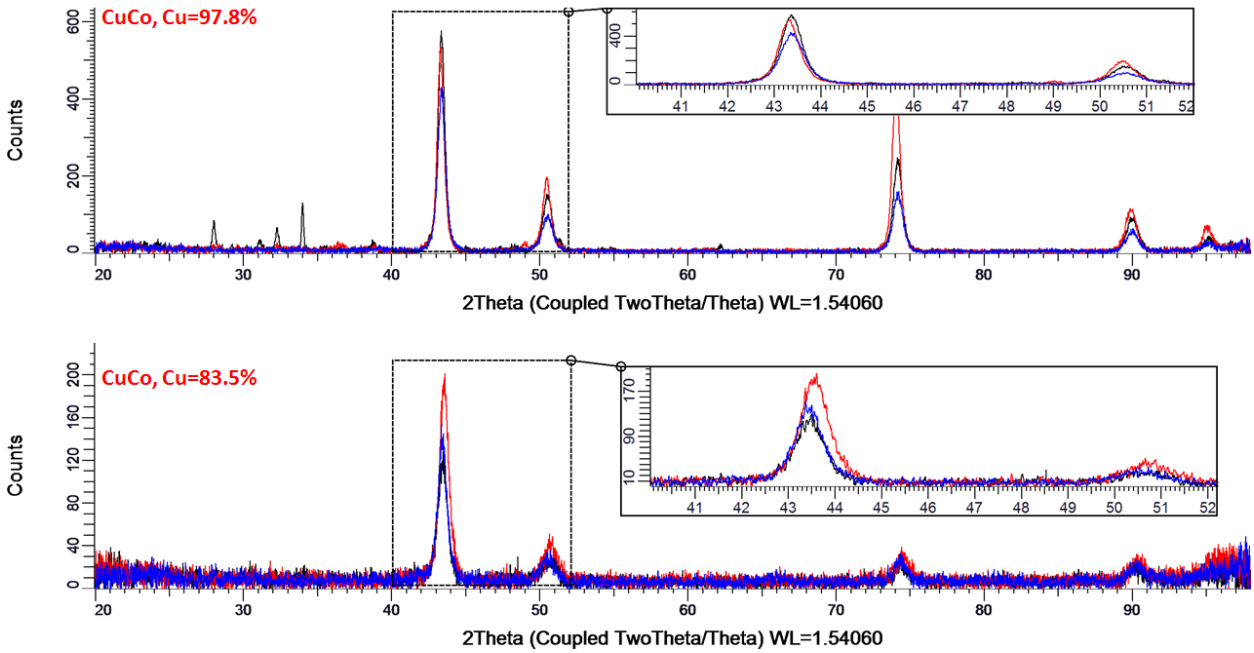

Figure S13: XRD for alloy CuCo before and after electrolysis. Blue: pristine, red: absence of additive, and black: presence of additive. The slight shift of peak position is due to slight sample composition variation from sample to sample and is estimated to be < 1% for the Cu-rich catalysts and < 2% for the Cu-poor catalysts.

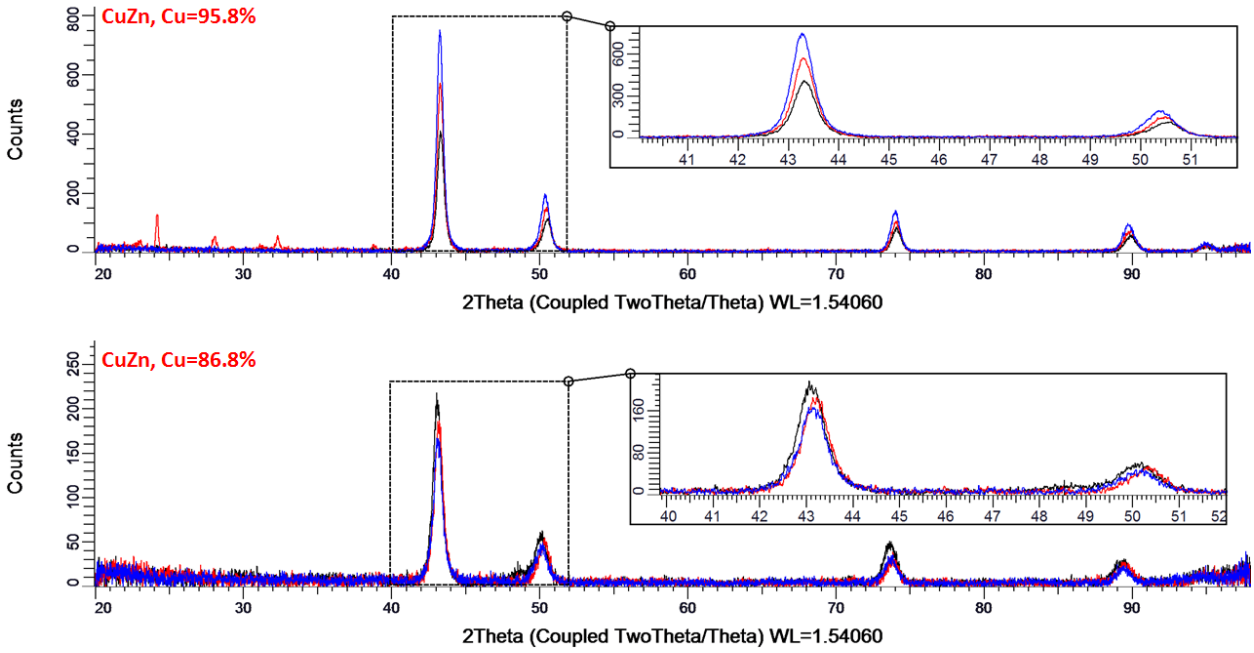

Figure S14: XRD for alloy CuZn before and after electrolysis. Blue: pristine, red: absence of additive, and black: presence of additive. The slight shift of peak position is due to slight sample composition variation from sample to sample and is estimated to be < 1% for the Cu-rich catalysts and < 2% for the Cu-poor catalysts.

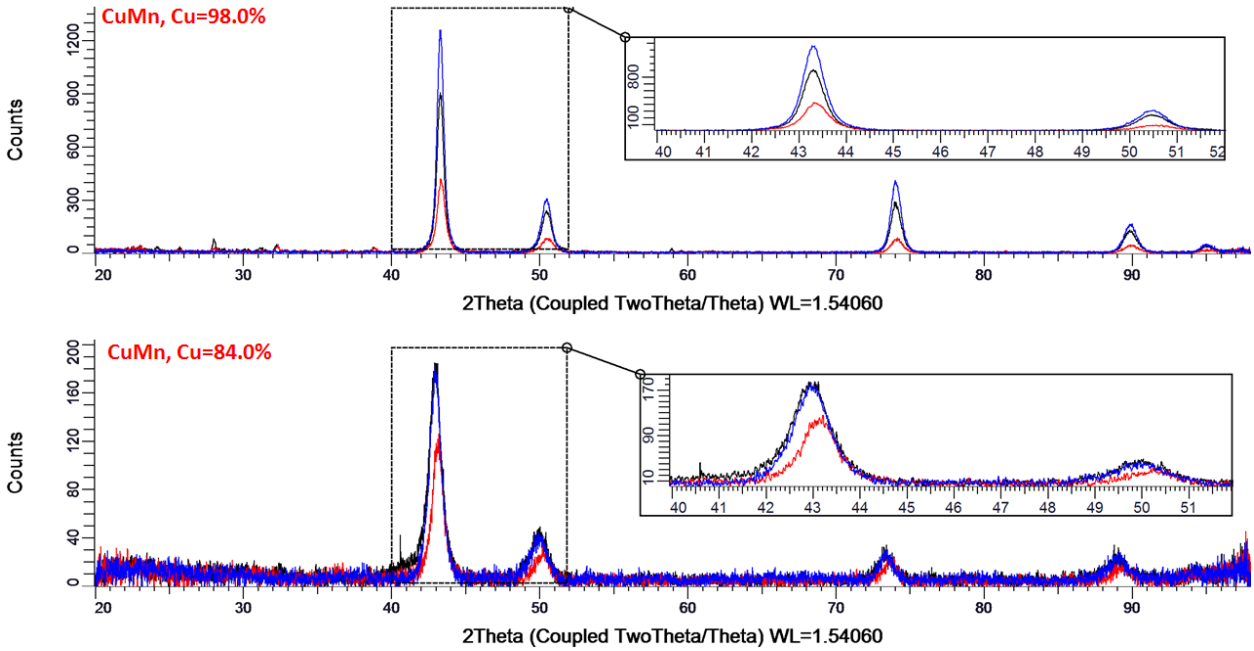

Figure S15: XRD for alloy CuMn before and after electrolysis. Blue: pristine, red: absence of additive, and black: presence of additive. The slight shift of peak position is due to slight sample composition variation from sample to sample and is estimated to be < 1% for the Cu-rich catalysts and < 2% for the Cu-poor catalysts.

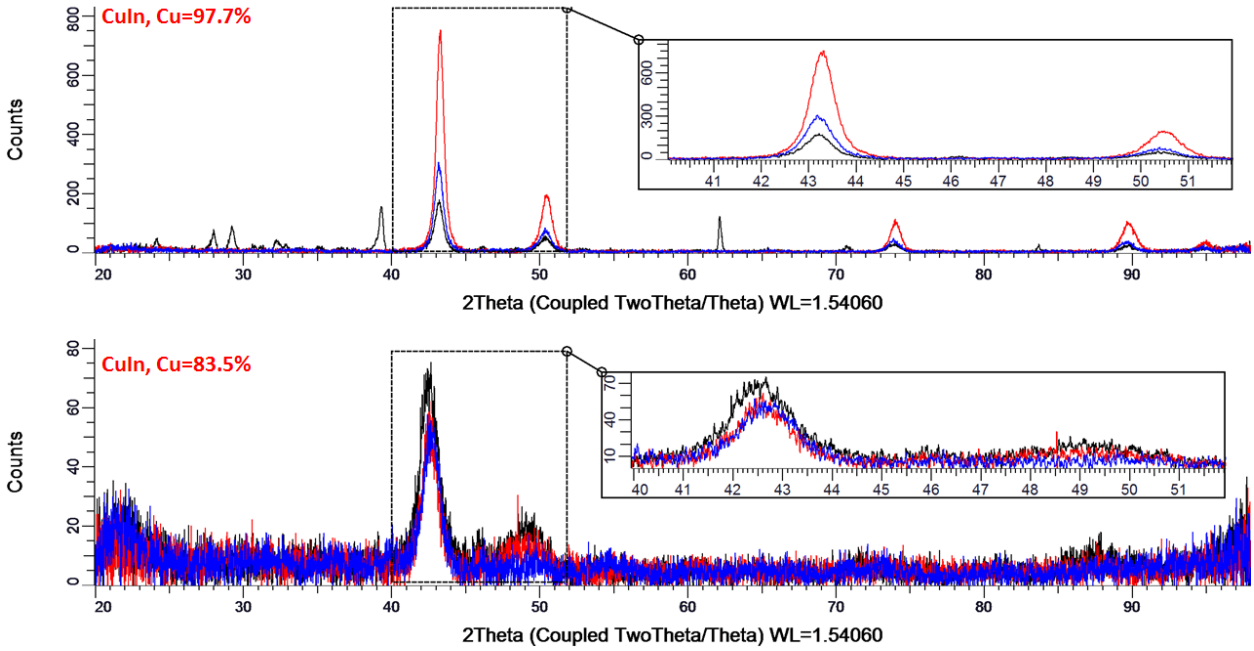

Figure S16: XRD for alloy CuIn before and after electrolysis. Blue: pristine, red: absence of additive, and black: presence of additive. The slight shift of peak position is due to slight sample composition variation from sample to sample and is estimated to be < 1% for the Cu-rich catalysts and <2% for the Cu-poor catalysts.

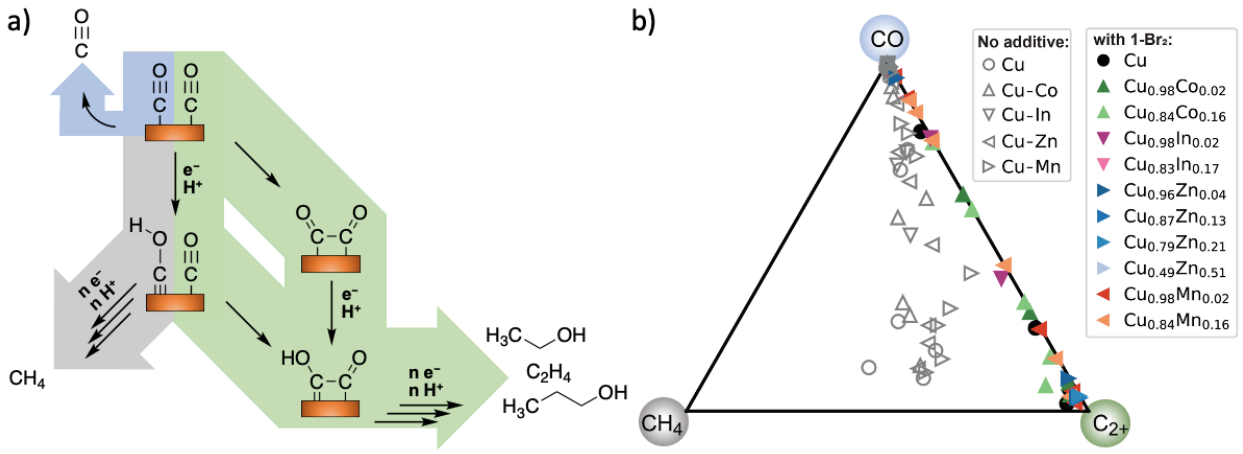

Figure S17: A complementary figure for Figure 3 in the main text.

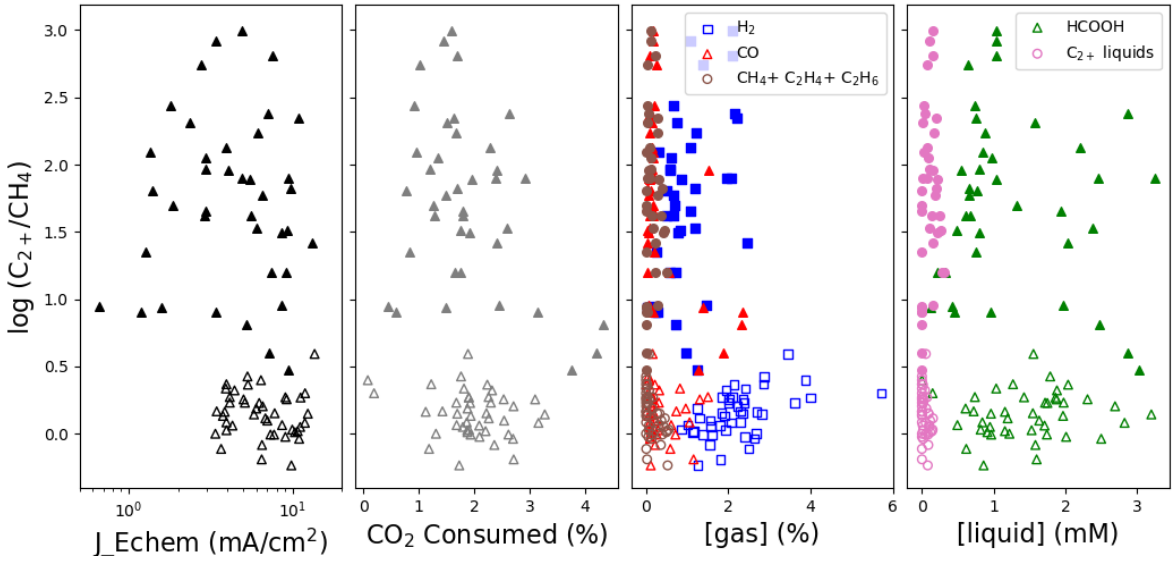

Figure S18: Electrochemical current density, CO_2 consumption (in the headspace) at the end of electrolysis, gas product concentration, and liquid product concentration vs log (C_{2+}/CH_4). Solid symbol: electrolyses with additive; hollow symbol: electrolyses without additive in 0.1 M $KHCO_3$.

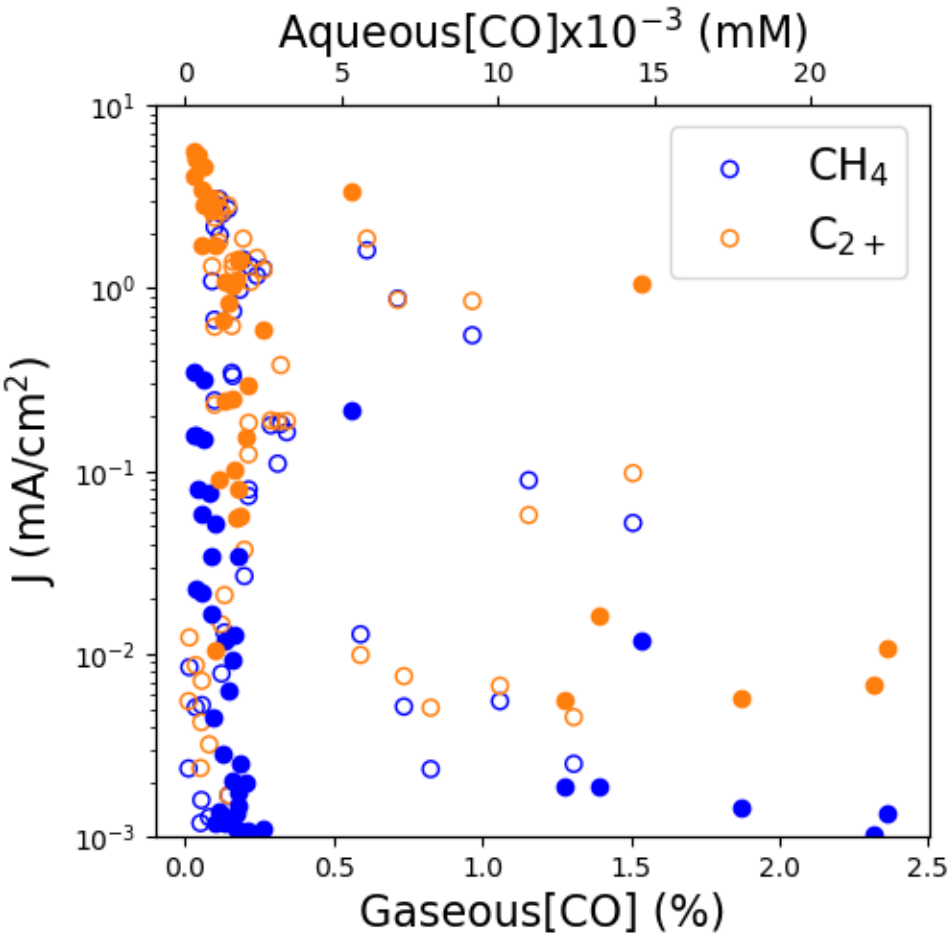

Figure S19: Product CO concentration vs partial current density of CH_4 and C_2H_4. The gaseous (headspace) CO concentration was measured by GC at the end of each electrolysis, while aqueous CO was estimated from the measured CO by Henry's law. Solid symbol: electrolyses with additive; hollow symbol: electrolyses without additive in 0.1M $KHCO_3$.

References

(1) Lai, Y.; Jones, R. J. R.; Wang, Y.; Zhou, L.; Gregoire, J. M. Scanning Electrochemical Flow Cell with Online Mass Spectroscopy for Accelerated Screening of Carbon Dioxide Reduction Electrocatalysts. *ACS Comb. Sci.* **2019**, *21* (10), 692–704. https://doi.org/10.1021/acscombsci.9b00130.

(2) Jones, R. J. R.; Wang, Y.; Lai, Y.; Shinde, A.; Gregoire, J. M. Reactor Design and Integration with Product Detection to Accelerate Screening of Electrocatalysts for Carbon Dioxide Reduction. *Rev. Sci. Instrum.* **2018**, *89* (12), 124102. https://doi.org/10.1063/1.5049704.

(3) Clark, E. L.; Singh, M. R.; Kwon, Y.; Bell, A. T. Differential Electrochemical Mass Spectrometer Cell Design for Online Quantification of Products Produced during Electrochemical Reduction of CO_2. *Anal. Chem.* **2015**, *87* (15), 8013–8020. https://doi.org/10.1021/acs.analchem.5b02080.

(4) Garza, A. J.; Bell, A. T.; Head-Gordon, M. Mechanism of CO2 Reduction at Copper Surfaces: Pathways to C2 Products. *ACS Catal.* **2018**, *8* (2), 1490–1499. https://doi.org/10.1021/acscatal.7b03477.

(5) Nitopi, S.; Bertheussen, E.; Scott, S. B.; Liu, X.; Engstfeld, A. K.; Horch, S.; Seger, B.; Stephens, I. E. L.; Chan, K.; Hahn, C.; Nørskov, J. K.; Jaramillo, T. F.; Chorkendorff, I. Progress and Perspectives of Electrochemical CO_2 Reduction on Copper in Aqueous Electrolyte. *Chem. Rev.* **2019**, *119* (12), 7610–7672. https://doi.org/10.1021/acs.chemrev.8b00705.

(6) Thevenon, A.; Rosas-Hernández, A.; Peters, J. C.; Agapie, T. In-Situ Nanostructuring and Stabilization of Polycrystalline Copper by an Organic Salt Additive Promotes Electrocatalytic CO_2 Reduction to Ethylene. *Angew. Chem. Int. Ed.* **2019**, *58* (47), 16952–16958. https://doi.org/10.1002/anie.201907935.